Cathodic corrosion

Hersbach, T.J.P.

4

Alkali Metal Cation Effects in Structuring Pt, Rh and Au Surfaces through Cathodic Corrosion

Cathodic corrosion is an electrochemical etching process which alters metallic surfaces by creating nanoparticles and a variety of etching features. Because these features typically have a preferential orientation, cathodic corrosion can be applied to modify and nanostructure electrode surfaces. However, this application of cathodic corrosion is currently limited by an insufficient chemical understanding of its underlying mechanism. This includes the role of alkali metal cations, which are thought to be crucial in both enabling cathodic corrosion and controlling its final facet preference. This work addresses this knowledge gap by exploring the cathodic corrosion of Pt, Rh and Au in LiOH, NaOH and KOH through both experimental and theoretical methods. These methods demonstrate that cations are adsorbed during cathodic corrosion and play a major role in controlling the onset potential and final surface morphology in cathodic corrosion. Interestingly, an equally significant role appears to be played by adsorbed hydrogen, based on calculations using literature density functional theory data. Considering the significance of both hydrogen and electrolyte cations, it is hypothesized that cathodic corrosion might proceed via an intermediate ternary metal hydride. This fundamental insight leads to both metal-specific recommendations and more general guidelines for applying cathodic corrosion to structure metallic surfaces.

4.1 Introduction

Cathodic corrosion is an enigmatic etching process that decomposes metallic cathodes at potentials where they are typically assumed to be cathodically protected. This decomposition leads to striking changes in the electrode surface, including the formation

This chapter is based on Hersbach, T. J. P., McCrum, I. T., Anastasiadou, D., Wever, R., Calle-Vallejo, F. & Koper, M. T. M., *ACS Applied Materials & Interfaces* **10**, 39363–39379 (2018).

of nanoparticles and geometric etch pits. Though these remarkable changes were already observed in the early 20th century[1] and briefly studied in the 1970s,[2] most fundamental studies of cathodic corrosion have been conducted relatively recently.[3–5] From these studies, it has been hypothesized that cathodic corrosion proceeds by forming an unknown metastable metal-containing anion,[6] instead of being caused by physical processes like contact glow discharge.[7] However, the exact nature of this (anionic) cathodic corrosion intermediate remains unclear. This limits fundamentally guided approaches towards applying cathodic corrosion to alter metallic surfaces and produce shape-controlled nanoparticles that exhibit favorable catalytic properties.[8] Such approaches would require more knowledge on the underlying mechanism and the different species involved in cathodic corrosion.

Perhaps the most crucial species in enabling cathodic corrosion is the electrolyte cation: without the presence of cations like Na^+, cathodic corrosion does not take place.[6] This key role of cations was underscored by several follow-up studies on nanoparticle production through cathodic corrosion, which reported effects of both the concentration and identity of the electrolyte cation on the corrosion rate,[9] particle size[9–11] and particle shape.[9,12,13] In terms of particle shape, these experiments found the (100)-to-(110) facet ratio to increase with increasing cation concentration,[9,12,13] and being higher for particles produced in 10 *M* NaOH compared to 10 *M* KOH.[12] These observations were tentatively ascribed to selective stabilization of (100) surface facets by Na^+ adsorption;[13] Na^+ would mimic the structure-influencing effect that other adsorbates exhibit in traditional nanoparticle synthesis methods.[14] In spite of the pronounced effect of Na^+, these observations were made for alternating current (AC) corrosion experiments, which accelerate the effects of cathodic corrosion by introducing periodic anodic corrosion steps. Though this approach is ideal for nanoparticle production, the convoluted presence of anodic and cathodic corrosion processes hinders explicit conclusions on the role of Na^+.

This ambiguity was alleviated by two subsequent studies on electrodes that were corroded under constant polarization (Chapter 2 & 3). These studies found that cathodic corrosion in 10 *M* NaOH preferentially forms (100) sites on Pt and Rh and (111) sites on Au. By exploring this difference between Au on the one hand and Pt and Rh on the other hand with density functional theory (DFT) calculations (Chapter 3), sodium was shown to adsorb most favorably on the type of step that matches the type of site formed: (100) for Pt & Rh, and (111) for Au. These results therefore align with the results for AC corrosion by suggesting a crucial role of the electrolyte cation in determining the facet preference

for cathodic corrosion. However, a systematic study of the extent of this cation effect on various metals has previously not been conducted. Such a study would not only provide fundamental insights on cathodic corrosion, but would also provide concrete guidelines for using cathodic corrosion as a tool to structurally alter metallic electrodes.

Therefore, this chapter provides such a study by mapping the corrosion behavior of Pt, Rh and Au in various concentrations of LiOH, NaOH and KOH. The experiments indicate a key role of the electrolyte cations in controlling the corrosion onset potential, as well as the final surface area and facet distribution of the corroded electrodes. Though these results do not allow us to determine a single reaction mechanism with certainty, the calculations do provide strong indications for the presence of adsorbed cations during cathodic corrosion. Additional calculations based on literature DFT data indicate an additional role of adsorbed hydrogen in determining the onset potential of cathodic corrosion. Given the suggested role of both adsorbed hydrogen and adsorbed cations, we will argue that the elusive cathodic corrosion reaction intermediate might be a ternary metal hydride.

These results are relevant from both fundamental and applied perspectives. On the one hand, the suggested existence of ternary metal hydrides provides a concrete starting point for future fundamental studies and is therefore an important clue towards understanding the chemical nature of cathodic corrosion. On the other hand, the exploration of cathodic corrosion as a function of the corroded metal and the identity and concentration of electrolyte cations provides valuable guidelines for applying cathodic corrosion to systematically modify electrode surfaces and create shape-controlled nanoparticles.

4.2 Materials and methods

4.2.1 Experimental methods

All water used in this study was demineralized and filtered by a MilliQ water system to reach a final total organic carbon (TOC) content below $5\ ppb$ and a resistivity above $18.2\ M\Omega \cdot cm$. To further ensure cleanliness, both organic and inorganic contaminations were removed from the glassware before each experiment. Organic contaminations were decomposed by storing glassware overnight in an aqueous solution of $1\ g \cdot L^{-1}$ $KMnO_4$ (Fluka, ACS reagent) and $0.5\ M$ H_2SO_4 (Fluka, ACS reagent). After storage, the solution was drained from the glassware and any remaining $KMnO_4$ was removed with dilute H_2O_2 (Merck, Emprove exp). Finally, the glassware was boiled 5 times in water before

being filled with electrolyte solution. All electrolytes were purged from oxygen before experiments by bubbling argon (Linde, 6.0 purity) through the solution for 30 minutes. Deoxygenation was maintained during experiments by flowing Ar over the solution. Electrochemical experiments were performed using a Bio-Logic SP-300 potentiostat.

In this study, two types of electrochemical cells were used: a glass cell for electrode characterization in acidic solution and a fluorinated ethylene propylene (FEP) cell for cathodic corrosion in alkaline solution. The glass cell contained an internal reversible hydrogen electrode (RHE) as reference electrode. The counter electrode was either a Pt spiral for Pt and Rh characterization or an Au spiral for Au characterization. In addition, a Pt or Au wire was connected to the reference electrode with a $4.7\ \mu F$ capacitor to filter high-frequency noise during voltammetry.[15] Working electrolytes consisted of H_2SO_4 (Merck, Ultrapur) in concentrations of $0.5\ mol \cdot L^{-1}$ for Pt or $0.1\ mol \cdot L^{-1}$ for Rh and Au characterization. The FEP cell contained a commercial HydroFlex RHE electrode (Gaskatel), a Ti spiral counter electrode (Mateck, 99.99%) and aqueous electrolytes of either dissolved $LiOH \cdot H_2O$ (Alfa Aesar, 99.995%), NaOH (Merck, Suprapur) or $KOH \cdot H_2O$ (Fluka, TraceSelect).

The Ti counter electrode provides the important benefit of not being any of the studied working electrode materials. As such, the results presented in this work cannot be attributed to redeposition of dissolved Pt, Rh or Au from the anodically polarized counter electrode. However, the use of a Ti counter electrode caused a noteworthy complication for cathodic corrosion, which we found to be very sensitive to the presence of unintended contaminations: for unknown reasons, the Ti counter electrode would occasionally shift the onset potential of cathodic corrosion of platinum to less negative potentials by as much as $0.3\ V$ from the value reported in Chapter 2. This issue could generally be solved by performing ten minutes of pre-electrolysis at $-1\ V$ *vs.* RHE with a Pt electrode (Mateck, 99.99%; $\varnothing = 0.1\ mm$), which was removed under potential control and discarded. Though this protocol adequately resolved the issue of early and significant cathodic corrosion, results of Pt corrosion were reproduced with a Pt counter electrode where necessary to confirm the validity of the presented onset potentials and the proper functioning of the working setup.

After preparing the working setup, Pt electrodes were prepared by cutting a short length of wire (Mateck, 99.99%; $\varnothing = 0.1\ mm$) from a spool with clean wire cutters and flame annealing the electrode. Rh (Mateck, 99.9%; $\varnothing = 0.125\ mm$) and Au (Materials Research Corporation, März Purity; $\varnothing = 0.125\ mm$) wires could not be annealed before

experiments and were cleaned chemically by immersion in a 1:3 volumetric mixture of 35% H_2O_2 (Merck, Emprove exp) and 95–97% H_2SO_4 (Fluka, ACS reagent) for 30 seconds instead, as was done in Chapter 3. Au wires were then also polished electrochemically by running 200 cyclic voltammograms (CVs) between 0 and $1.75\ V$ *vs.* RHE at a scan rate of $1\ V \cdot s^{-1}$ in the characterization cell.[16]

After preparation, each electrode was immersed in the characterization cell at a depth that was carefully controlled by using a micrometer screw. In the characterization cell, the electrode surface was characterized by running 4 cyclic voltammograms. Following characterization, the electrode was rinsed and moved into the FEP cell. Here, an 85% ohmic drop-corrected constant cathodic voltage was applied for 60 seconds, after which the electrode was removed under potential control. After an additional rinse, the electrode was moved back into the characterization cell, immersed at the same depth as during the initial characterization and re-characterized by running 4 CVs. Finally, the electrode was stored for later characterization using scanning electron microscopy.

Scanning electron microscopy was carried out on a FEI NOVA NanoSEM 200 microscope, using an acceleration voltage of $5\ kV$ and an electron beam current of $0.9\ nA$. All samples were mounted to be aligned vertically in the presented micrographs, to within an error of several degrees.

4.2.2 Theoretical methods

We used density functional theory to examine the specific adsorption of alkali metal cations (Li, Na, and K) onto the (111), (100), (211), and (553) surfaces of Rh, Pt, and Au in the presence of near-surface solvation. The Vienna Ab Initio Simulation Package (VASP) was used to perform the electronic structure calculations,[17–19] with a plane-wave basis set and the Perdew-Burke-Ernzerhof (PBE) exchange-correlation functional.[20,21] Ion-core potentials were modeled using the projector augmented wave (PAW) approach.[22,23] The basis set cutoff energy was $450\ eV$. Structural optimization was performed until the forces on the atoms were below $0.02\ eV \cdot Å^{-1}$. Adsorption was modeled at only one coverage. The (111) surface was modeled with a 3×3 unit cell (with 3 alkali metal cation adsorbates giving a 1/3 monolayer (ML) coverage), the (100) surface with a 2×2 unit cell (with 1 alkali metal cation adsorbate, 1/4 ML coverage), and the (211) and (553) surfaces in a 2×1 unit cell (containing a two-atom-wide step edge, with one alkali metal cation adsorbate). K-space sampling was performed with a $5 \times 5 \times 1$ Monkhorst-Pack mesh grid for the (111) surfaces of Rh and Pt and a $7 \times 7 \times 1$ grid for all of the other surfaces

of Rh and Pt.[24] The Au surfaces were sampled with a denser grid, $7 \times 7 \times 1$ for Au(111), $11 \times 11 \times 1$ for Au(100), $15 \times 11 \times 1$ for Au(553), and $11 \times 15 \times 1$ for Au(211). Adsorption energies on each surface were converged to within 0.03 eV with respect to the k-space sampling. Each of the surfaces was modeled with a four-layer slab, with the bottom two layers frozen at the DFT-calculated lattice constant. Dipole corrections were included in the surface normal direction.[25]

Cation adsorption potentials were calculated following methods described previously, including the effect of near-surface water solvation.[26,27] For the (111) surface, six explicit water molecules were included in a bilayer structure; for the (100), (211), and (553) surfaces, four explicit water molecules were added in a hydrogen-bonded monolayer adsorbed on the surface (or step edge, in the case of the stepped surfaces). Only one water structure was considered on each surface, which was relaxed in the absence and presence of the alkali metal cation. The initial water structures have been found previously (on Pt) to be low or minimum energy structures: on the (111) surfaces, a hexagonal bilayer water structure was used;[28,29] on the (100) surfaces, a square-like arrangement of water molecules was used;[30] and on the stepped surfaces, a double-stranded structure was used.[31] Images of these structures, in the absence and presence of an alkali metal cation, are given in Fig. A.1–A.3. Images of the adsorbate structures were rendered using VESTA.[32]

This method approximates effects of solvation, since we can only identify water structures near the surface and the adsorbed cation that are at a local (but not necessarily global) minimum in energy, and we neglect translational and rotational entropy of the near-surface water (considering only vibrational energy and entropy). Our intent is therefore to only approximate the effects of near-surface solvation on the alkali metal cation adsorption energy. In our prior work, we found this energy to reach a plateau after solvating the adsorbed cation with four to six water molecules:[26] approximately the number of water molecules in the solvation shell of bulk, solution-phase alkali atoms, as found previously using *ab-initio* molecular dynamics.[33] We found previously that the addition of more water molecules causes the absolute alkali metal adsorption energy to fluctuate by $\pm 0.5\ eV$ per water molecule. We therefore expect our absolute adsorption energy accuracy to not be better than $\pm 0.5\ eV$. The error in the relative adsorption energy trend between cations is smaller.

Adsorption energies were also calculated in the absence of near-surface solvation and relative to gas phase, neutral alkali metal atoms, following the method described in

Chapter 3. These calculations neglect the stabilizing effect of solvent on both the reactant and adsorbed product states. This alters both the absolute adsorption energetics and the trend between the cations, because the degree of lost solvation upon adsorption is cation-dependent. These adsorption energies are given in the Fig. A.30–A.31, and allow for separate examination of the contribution of the solvation effects on adsorption. Fig. A.30–A.31 can be compared with the adsorption energetics in this chapter, which are all calculated using an aqueous solution-phase ion as the initial state.

Cation effects have been explained as being caused by the behavior of cations in the double-layer or outer Helmholtz plane, near the electrode surface.[34] However, we here examine the conditions under which some of these cations approach the electrode surface more closely and lose part of their solvation shell. This allows them to be considered "specifically adsorbed". Our current and previous calculations therefore support that such adsorption is favorable at low potentials and high pH,[26,35] where alkali cation adsorption becomes increasingly favorable compared to hydrogen adsorption.

We have also examined the stability of the (111) and (100) surfaces of Rh, Pt, and Au in the presence of high coverages of adsorbed hydrogen, using bare surface energies calculated using DFT by Tran *et al.*,[36] as well as hydrogen adsorption energies calculated using DFT at low coverage ($0.25\ ML$) by Ferrin *et al.*[37] To estimate the adsorption energy of hydrogen at high coverages, we assumed a simple mean-field model using a constant, repulsive, coverage dependence of the hydrogen adsorption energy of $0.12\ eV \cdot ML^{-1}$ on the (111) surfaces of Rh, Pt, and Au. This repulsive interaction has been explicitly calculated on Pt(111);[27,38] the same coverage dependence was assumed on Rh(111) and Au(111). It should be noted that Skúlason *et al.* show a slightly greater repulsion on Au(111) and weaker repulsion on Rh(111) than on Pt(111).[39] Consideration of these differences would yield a small change in the calculated surface energetics at low potentials (high hydrogen coverages). However, this change would only emphasize the trend in which (111) surface is the most stable (Rh > Pt > Au). As such, including these small differences in binding energy will not affect our conclusions. We also assume that adsorption between low and high coverage ($1\ ML$) on the (100) surfaces is independent of coverage on Rh(100), Pt(100), and Au(100), as has been found for Pt(100).[27,38]

Potential-dependent surface energies (with $1\ ML$ hydrogen adsorbed on the surface) were calculated as described previously, by adding the potential-dependent adsorption energy of hydrogen (normalized by surface area) to the surface energy of the

bare surface.[40] This procedure is outlined in Equations 4.1 and 4.2:

$$\gamma(U_{RHE}, \theta_{*H}) = \gamma_{bare} + \frac{\Delta G_{H_{ads}}(U_{RHE}, \theta_{*H})}{A} \tag{4.1}$$

$$\begin{aligned}\Delta G_{H_{ads}}(U_{RHE}, \theta_{*H}) = BE(\theta_{*H} = 0.25ML) + 0.5\Delta H_{H_2}^{form} + \\ \Delta ZPVE_{H_{ads}} - T\Delta S_{H_{ads}} + n|e|U_{RHE} + \omega\theta_{*H}\end{aligned} \tag{4.2}$$

Here, $\gamma(U_{RHE}, \theta_{*H})$ is the surface energy of the hydrogen-covered surface as a function of potential (on a reversible hydrogen electrode scale, RHE) and hydrogen coverage (θ_{*H}); γ_{bare} is the surface energy of the bare surface;[36] A is the area of the surface; $\Delta G_{H_{ads}}(U_{RHE}, \theta_{*H})$ is the free energy of hydrogen adsorption; BE is the binding energy of hydrogen on the surface at low coverage ($0.25\ ML$);[37] $\Delta H_{H_2}^{form}$ is the formation enthalpy of hydrogen gas at standard state ($-4.57\ eV$);[37] $\Delta ZPVE_{H_{ads}}$ is the change in zero point vibrational energy of the hydrogen upon adsorption ($-0.008\ eV$);[38] $T\Delta S_{H_{ads}}$ is the change in entropy of the hydrogen upon adsorption ($-0.00067\ eV \cdot K^{-1}$);[38] n is the number of hydrogen atoms adsorbed in the unit cell at the coverage of interest; $|e|U_{RHE}$ is the energy of an electron on the reversible hydrogen electrode scale; and ω is the *H-*H interaction term describing the interaction between adsorbed hydrogen on the surface ($0.12\ eV \cdot ML^{-1}$ for *H on Pt(111), $\sim 0\ eV \cdot ML^{-1}$ for *H on Pt(100)).[27,38] This difference in interaction energy is consistent with experimental estimates that indicate weaker (but non-zero) H-H interactions for Pt(100) than for Pt(111).[41,42] We assumed complete electron transfer between the adsorbing proton and the surface, so that all of the potential dependence arises from the electron being transferred as a reactant on proton adsorption. Additionally, we neglected the effects of near-surface solvation and electric field on hydrogen adsorption, since these effects have been shown previously to be small.[38]

As we have found hydrogen adsorption above 1 ML (up to 1.25 ML) on Pt(100) to be favorable at low but positive potentials (near 0.1 V *vs.* RHE),[40] we have extrapolated and included these data as well. Besides, we calculated the adsorption energy of hydrogen at 1.25 ML on Rh(100) using the same methods defined previously for *H adsorption on Pt(100).[40] For this calculation, we used the PBE exchange-correlation functional, as was used to examine alkali metal cation adsorption. We find that the additional 0.25 ML hydrogen prefers to adsorb in a bridge site (as do the hydrogen atoms between 0 and 1 ML) on Rh(100). As hydrogen adsorption is significantly weaker on Au(100) than on Pt(100) and Rh(100), a higher coverage (1.25 ML) was not considered on this surface.

While the bare surface energies are particularly sensitive to the functional used and the level of convergence defined, the relative stability of the (111) and (100) facets of each metal should be less sensitive. We therefore expect the trend in surface energies between (111) and (100) to be robust.

4.3 Results and discussion

In the following section, we will first describe the experimentally studied corrosion behavior of Pt, Rh and Au in LiOH, NaOH and KOH electrolytes. This description will be separate for each metal and will focus on the difference in corrosion behavior as a function of the electrolyte composition. This approach differs slightly from Chapter 2 & 3, which mainly described the corrosion behavior as a function of the corrosion potential. However, an electrochemical impression of the corrosion behavior as a function of the applied potential can be gained from Fig. A.4 through Fig. A.15 in Appendix A, which correspond to the figure format used in Chapter 2 & 3. Similarly, Fig. A.16 through Fig. A.27 display scanning electron micrographs of the electrodes as a function of the applied potential. Since Fig. A.4 through Fig. A.27 are designed to complement the figures in this chapter, the interested reader is referred to these supporting figures for a more complete impression of the experimental results on the corrosion behavior of the studied systems. These figures in the appendix are also accompanied by additional discussion of the presented results and conclusions.

After describing the experimental results, we will proceed by presenting our complementary theoretical results on the adsorption of Li, Na, K and H on Pt, Rh and Au. The experimental and theoretical results will be further interpreted and connected in the Discussion section.

4.3.1 Results

Experimentally determined corrosion behavior

The corrosion behavior of Pt, Rh and Au was studied through both cyclic voltammetry (CV) and scanning electron microscopy (SEM). As in the previous chapters, the metallic electrodes were treated by applying a constant cathodic voltage *versus* an internal reversible hydrogen electrode (RHE) for 60 seconds in a concentrated alkali metal hydroxide solution. Before and after this cathodic polarization, the electrodes were characterized by cyclic voltammetry in a sulfuric acid solution to monitor changes in the structure of the

electrode surface. Additionally, the electrodes were imaged by SEM after corrosion to identify etching features in the surface.

In these experiments, the applied corrosion potentials are purposefully spaced by 0.1 V steps: the smallest interval at which we believe that differences in corrosion behavior can reliably be assessed with the current methodology. Given this potential spacing, our resolution in determining corrosion onset potentials is 0.1 V. Strictly speaking, this means that the 'true' corrosion onset potential will lie between the most negative potential where no corrosion can be detected and the least negative potential where corrosion can be detected. For consistency, however, we will follow Chapter 2 & 3 in defining the corrosion onset potential as the least negative potential where corrosion can be detected. This detection will rely predominantly on cyclic voltammetry.

Platinum

For platinum, the use of cyclic voltammetry is well established as a quick and reliable method for characterizing electrode surfaces. This characterization relies on the so-called 'hydrogen region', which in 0.5 M H_2SO_4 contains the following anodic features that are important for this work:[43]

1. A peak at 0.13 V *vs.* RHE, corresponding to the substitution of *H by *OH on (110)-type sites.[44,45]

2. A peak at 0.27 V *vs.* RHE, corresponding to (100)-type step sites near terrace borders.[44,45]

3. A broader feature between 0.3 and 0.4 V *vs.* RHE, corresponding to (100) terrace sites.

4. A broad feature between 0.06 and 0.3 V *vs.* RHE, corresponding to hydrogen desorption on (111) terraces. This feature is accompanied by a broad feature between 0.4 and 0.55 V *vs.* RHE, for (bi)sulfate adsorption on (111) terraces.

Since these features depend strongly on the presence and abundance of their corresponding surface sites, the use of cyclic voltammetry is extremely sensitive to small changes in the electrode structure. As such, CV measurements, complemented by SEM images, will be the primary method for quantifying the differences between corrosion in different electrolytes.

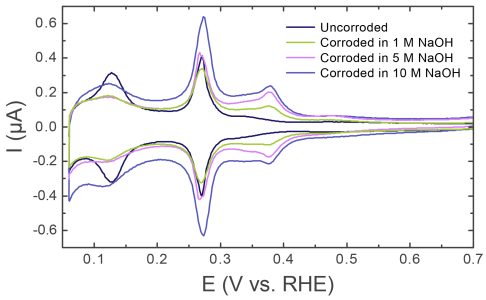

Fig. 4.1 | Cyclic voltammograms of Pt corroded in NaOH of various concentrations, at -1.0 *V vs.* RHE. Voltammograms were recorded in 0.5 *M* H_2SO_4, at a scan rate of 50 $mV \cdot s^{-1}$.

Electrolyte concentration

The differences are first explored as a function of cation concentration for NaOH electrolytes: in Fig. 4.1, voltammograms of electrodes corroded at -1 *V vs.* RHE in 1, 5 and 10 *M* NaOH are displayed in increasingly darker colors, with the uncorroded electrode displayed in dark blue. The comparison of these voltammograms reveals higher measured currents in the voltammograms of electrodes corroded in higher NaOH concentrations. This higher current corresponds to a larger hydrogen desorption charge, which in turn corresponds to more exposed surface area.[46] For the presented samples, this represents surface area increases of 28, 32 and 74% after corrosion in 1, 5 and 10 *M* NaOH, respectively. Higher electrolyte concentrations therefore induce more electrode roughening.

This increased roughness with increasing concentration correlates well with the corrosion onset potential. For Pt corrosion, this onset was shown in Chapter 2 to be signified by a decrease in (110) features at 0.13 *V vs.* RHE, which is accompanied by a minor increase in (100) features at 0.27 *V vs.* RHE. As can be seen in Fig. A.5 & A.8, these changes occur respectively after polarization at -0.6 *V vs.* RHE (-1.4 *V vs.* NHE) and -0.5 *V vs.* RHE (-1.4 *V vs.* NHE) in 1 and 5 *M* NaOH. These onset potentials are more negative than the -0.4 *V vs.* RHE (-1.3 *V vs.* NHE) observed in Chapter 2 for 10 *M* NaOH. This onset trend and the less substantial roughening in more dilute solutions indicate that the extent of corrosion correlates strongly with NaOH concentration.

Based on this trend as a function of concentration, one might expect the facet distribution to also change monotonically with regard to concentration. This is indeed the case for (100) features: both (100) step sites (0.27 *V vs.* RHE) and terrace sites (0.3–0.4 *V vs.*

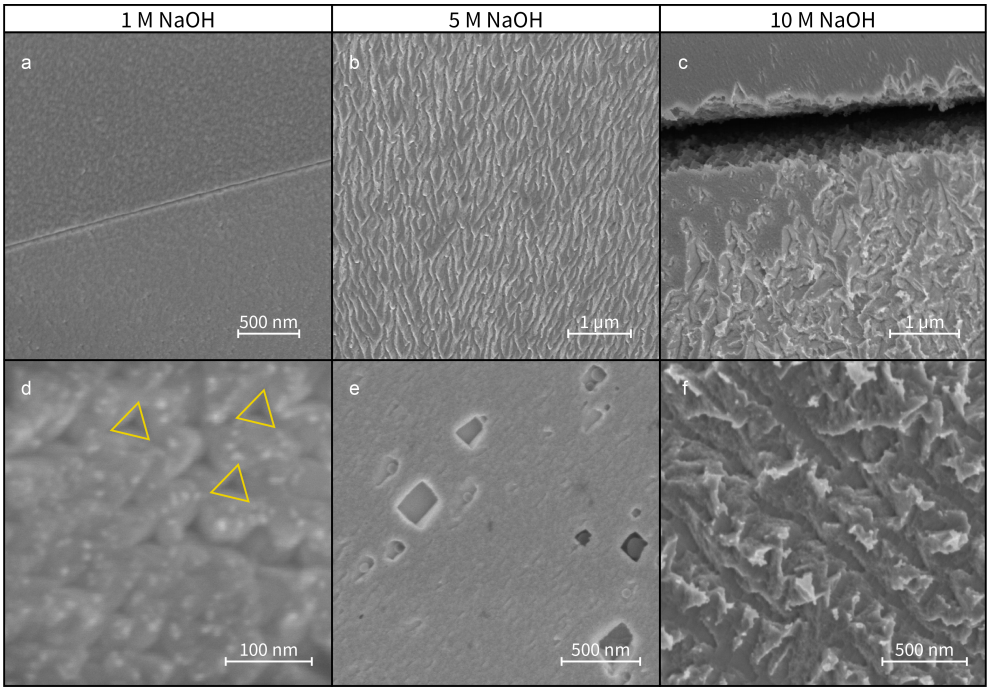

Fig. 4.2 | Scanning electron micrographs of Pt electrodes corroded at −1 *V vs.* RHE in 1 *M* NaOH **(a**, **d)**, 5 *M* NaOH **(b**, **e)** and 10 *M* NaOH **(c**, **f)**. Triangular features are highlighted in yellow.

RHE) increase with electrolyte concentration. However, the amount of (110) sites first decreases between 1 and 5 *M* NaOH, to then increase when corroding in 10 *M* NaOH. This indicates an interesting feature of cathodic corrosion in 10 *M* NaOH: the newly created surface area appears more disordered than that created at lower electrolyte concentrations, as is motivated in Appendix A.

Further indications of a rougher and more disordered surface follow from microscopy-based examination of the corroded electrodes, presented in Fig. 4.2. In this figure, Panels **a** and **d** display an electrode corroded in 1 *M* NaOH at −1.0 *V vs.* RHE. As can be seen in Panel **a**, which features the boundary between two crystal grains, the electrode appears predominantly roughened on the nano-scale, without the presence of well-defined etching features. However, small sections of the electrode feature triangular etch pits, which are (100)-oriented pits in (111)-like facets, as explained in Chapter 2 (model etch pit: Fig. A.28).

More severe corrosion features are present after cathodic treatment at −1 *V vs.* RHE

in 5 *M* NaOH (Fig. 4.2 **b**, **e**). This treatment causes the appearance of etch lines (Fig. 4.2 **b**) on large sections of the electrode and areas containing etch pits with more subtle roughening between them (Fig. 4.2 **e**). Many of these pits contain ~90-degree angles and are assigned to (100)-type sites. This assignment is based on Chapter 2, but is also illustrated here by a model etch pit (Fig. A.28).

Finally, when increasing the NaOH concentration to 10 *M* (Fig. 4.2 **c**, **f**), the etch features increase further in size, thus indicating higher roughness. These features (Fig. 4.2 **f**) contain edges that are less straight than those after corrosion in less concentrated solutions. As such, the SEM images support the electrochemical observation that the increase from 5 to 10 *M* NaOH induces the formation of more disordered sites on the nano-level. Similarly, the SEM results corroborate the electrochemically observed roughness increase with cation concentration.

Cation identity

Besides being sensitive to the cation concentration, cathodic corrosion also responds strongly to the cation identity. This is illustrated in Fig. 4.3, which explores Pt corrosion as a function of cation type for electrolyte concentrations of 1 *M* (Panel **a**, **b**) and 5 *M* (Panel **c**, **d**). This exploration is further subdivided in mildly negative potentials (Panel **a**, **c**) and more negative corrosion potentials (Panel **b**, **d**).

At mildly negative potentials, the electrolyte cation appears to barely affect the facet preference after corrosion. At these potentials, the cyclic voltammograms for corroded Pt overlap quite well: the amount of created (100) terraces is similar for all electrolytes of similar concentrations. This overlap is particularly noteworthy because the corrosion onset potentials, derived from Fig. A.4–A.9, are not the same for all types of cations. For 1 *M* KOH, the onset potential is −0.5 *V vs.* RHE (−1.3 *V vs.* NHE), while it is −0.6 *V vs.* RHE (−1.4 *V vs.* NHE) for 1 *M* NaOH and LiOH. Similarly, for 5 *M* electrolytes, the onset potential is −0.4 *V vs.* RHE (−1.3 *V vs.* NHE) for KOH and at −0.5 *V vs.* RHE (−1.4 *V vs.* NHE) for NaOH and LiOH. This indicates that, at mildly negative potentials, the final facet distribution does not necessarily correlate with the cation-influenced onset potential, but rather with the applied electrode potential.

This observation contrasts with the behavior at more negative potentials, which depends strongly on the nature of the electrolyte cation. For 1 *M* corrosion electrolytes (Fig. 4.3 **c**), this dependence shows a clear trend between cations: larger cations remove more (110) sites and create more (100) step and terrace sites. This facet preference trend

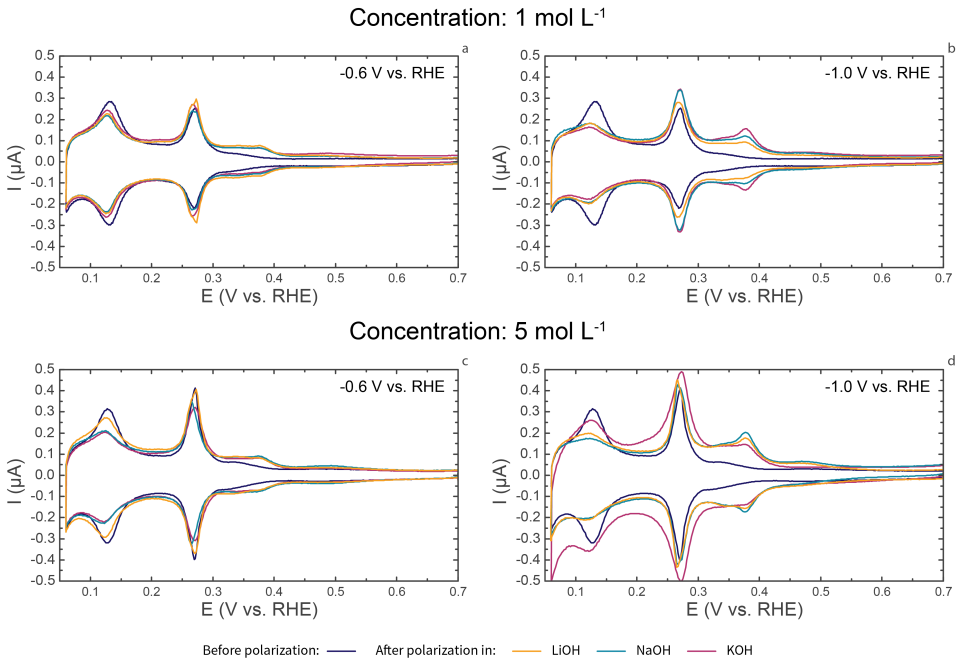

Fig. 4.3 | Cyclic voltammograms of Pt corroded in LiOH, NaOH and KOH at concentrations of 1 M **(a**, **b)** and 5 M **(c**, **d)**, at -0.6 V *vs.* RHE **(a**, **c)** and -1.0 V *vs.* RHE **(b**, **d)**. Voltammograms were recorded in 0.5 M H_2SO_4, at a scan rate of 50 $mV \cdot s^{-1}$.

is accompanied by a modest tendency for more surface area creation as the cation size increases.

The trend in surface area formation is sustained in more concentrated solutions, as can be seen in Fig. 4.3 **d**: at -1 V *vs.* RHE, most surface area is created in KOH solutions, followed respectively by NaOH and LiOH. Similarly, the facet preference trend is almost sustained in 5 M solutions. As in more dilute solutions, slightly more (100) terraces are created in NaOH electrolytes than in LiOH electrolytes. However, compared to these electrolytes, KOH causes an increase in (110) and (100) step sites and small decrease in (100) terraces. This increased step site formation is similar to that observed between 5 and 10 M NaOH. One can therefore also argue that moving from 5 M NaOH to 5 M KOH produces a more disordered surface after corrosion.

These electrochemical results can be analyzed in the light of scanning electron microscopy characterization. For 1 M electrolytes, SEM detects differences between cations,

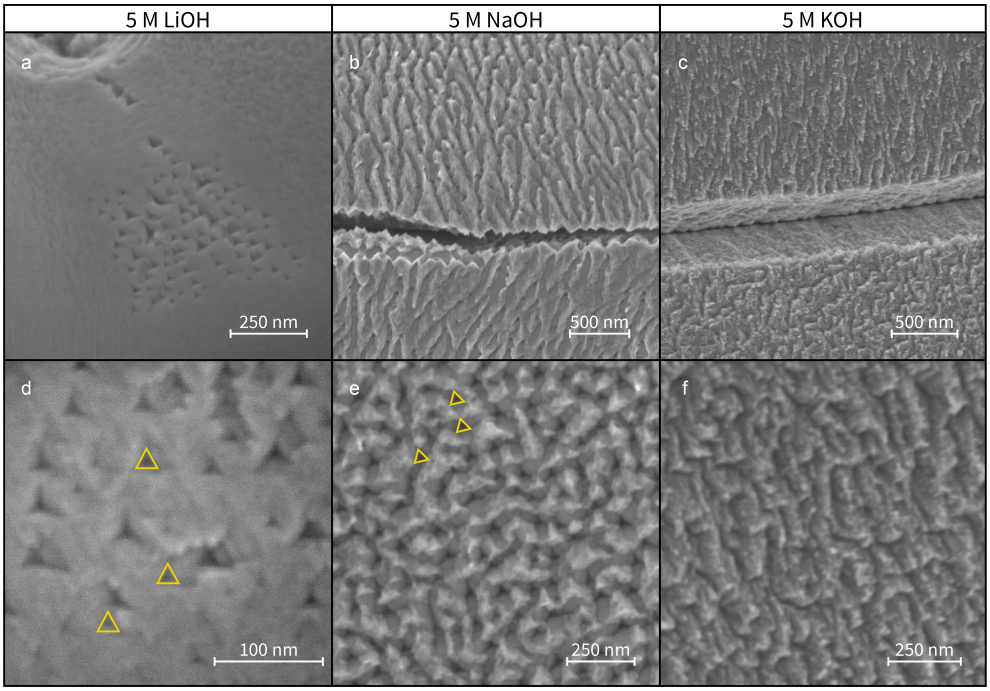

Fig. 4.4 | Scanning electron micrographs of Pt electrodes corroded at −1 *V vs.* RHE in *5 M* LiOH **(a**, **d)**, *5 M* NaOH **(b**, **e)** and *5 M* KOH **(c**, **f)**. Triangular features are highlighted in yellow.

with larger cations inducing more corrosion (Fig. A.16–A.18). This qualitatively matches the results in more concentrated electrolytes. As can be seen in Panels **a** and **d** of Fig. 4.4, corrosion in *5 M* LiOH causes the formation of (100)-type triangular etch pits. These pits are present on small areas of the electrode; in other areas, any corrosion features are beyond the resolution of the SEM (Fig. A.19).

This differs significantly from corrosion in *5 M* NaOH (Panels **b** and **e** of Fig. 4.2 and 4.4): etch lines are widespread and rectangular etch features can be seen in Fig. 4.2 **e**, underneath the grain boundary in Fig. 4.2 **b** and in Fig. A.20 **e**. In addition, the electrodes show significant corrugation that contains triangular features (Fig. 4.4 **e**), which resemble the triangular pits observed for less severe corrosion. These pits could serve as therefore initiation sites for more severe etching features, as is illustrated in Appendix A.

Finally, corroding in *5 M* KOH creates rougher and less well-ordered features than those observed for LiOH and NaOH: large troughs are found along grain boundaries (Fig. 4.4 **c**) and significant roughness without straight features is found on crystal grains

(Fig. 4.4 **f**).

These SEM and voltammetry results create a coherent impression of cathodic corrosion. Corrosion in LiOH creates the least amount of surface area. This area is only slightly smaller than that created in NaOH electrolytes, while the electrodes appear markedly different in SEM. This indicates that corrosion in LiOH electrolytes creates roughness on scales below the SEM resolution. Corrosion in NaOH electrolytes then causes more macroscopic roughness. This roughness contains well-developed electrochemical (100) terrace features that correspond with the formation of straight, long-distance features in SEM. Such well-ordered sites are mostly absent from electrodes corroded in 5 *M* KOH, which appear the roughest and most disordered in both voltammetry and electron microscopy.

As such, a clear effect of the cation is present for both studied electrolyte concentrations. At low concentrations, the cation predominantly affects the surface facet distribution, causing most (100) sites to be formed in KOH, followed respectively by NaOH and LiOH. At higher concentrations, corrosion in NaOH and LiOH induces well-developed (100) features, with KOH leading to an increased amount of step sites. Corrosion furthermore produces more surface area with increasing cation size.

Rhodium

In contrast with platinum voltammograms, rhodium voltammograms only feature one set of 'hydrogen' peaks.[47] Of this set, the cathodic peak corresponds to (bi)sulfate desorption, accompanied by hydrogen adsorption. Accordingly, the anodic peak corresponds to hydrogen desorption, accompanied by (bi)sulfate adsorption. The position of these peaks varies, depending on the exposed electrode facets. For the three basal planes, this yields the following peak positions in 0.1 *M* H_2SO_4:[47]

1. Rh(111) contains a sharp cathodic peak at 0.105 *V vs.* RHE and a sharp anodic peak at 0.122 *V vs.* RHE.

2. Rh(100) contains a sharp cathodic peak at 0.149 *V vs.* RHE and a sharp anodic peak at 0.157 *V vs.* RHE.

3. Rh(110) contains a broad cathodic peak at 0.107 *V vs.* RHE and a broad anodic peak at 0.120 *V vs.* RHE.

In line with our Chapter 3, we will primarily focus on the anodic peaks. The peaks are located around 0.121 V *vs.* RHE for the (111) and (110) facets, but situated approximately 35 mV more positive for the (100) facet. We used this peak position difference in Chapter 3 to determine the onset potential of rhodium: at the corrosion onset of -0.4 V *vs.* RHE (-1.3 V *vs.* NHE), the anodic hydrogen peak shifts positively by 2 mV. This positive shift signifies the formation of (100) sites. Because this peak shift is more abrupt than the gradual increase in electrode surface area, the same shift will be used here to determine the corrosion onset. We will focus exclusively on the effect of the cation identity in 5 M electrolytes, because cathodic corrosion of Rh in 1 M electrolytes is subtle and the spread in the data is too large to reliably establish onset potentials and facet preferences.

Cation identity

For 5 M electrolytes, the peak shift and surface area increase (as determined from the hydrogen desorption charge) after 60 seconds of cathodic polarization are presented in Fig. 4.5. In this figure, the anodic peak shift (Panel **b**) is approximately 2 mV in absence of cathodic corrosion. Though this 'baseline' shift is slightly higher than the < 1 mV shift in Chapter 3, it is reproducible for the presently studied electrolytes. The first electrolyte to exhibit a shift larger than 2 mV is 5 M KOH, for which a 4 mV peak shift marks the onset of cathodic corrosion at -0.4 V *vs.* RHE (-1.3 V *vs.* NHE). In agreement with Chapter 3, this 4 mV change represents an approximate 2 mV shift from the baseline change in peak position. Similar 3–4 mV total shifts occur at -0.5 V *vs.* RHE (-1.4 V *vs.* NHE) for LiOH and NaOH. These onset potentials match those for Pt corrosion, with corrosion in 5 M KOH starting at less negative potentials than corrosion in 5 M NaOH and LiOH.

Another similarity with Pt is that the initial surface area increase (Fig. 4.5 **a**) is similar at mildly negative potentials and starts diverging at approximately -0.7 V *vs.* RHE. However, the trend in surface area formation differs from platinum: most surface area is formed in NaOH, followed respectively by KOH and LiOH. Though the cause of this differing trend is unclear, it does match the observed peak shifts for Rh corrosion: the shift is highest for NaOH, with LiOH and KOH producing shifts that are 2 to 4 mV smaller, depending on the exact corrosion potential.

Such differences between cations in both surface area and peak shift are consistent with SEM characterization results, which are shown for the three electrolytes in Fig. 4.6. The electrolyte for which Fig. 4.5 **a** indicates the smallest surface area increase is 5 M

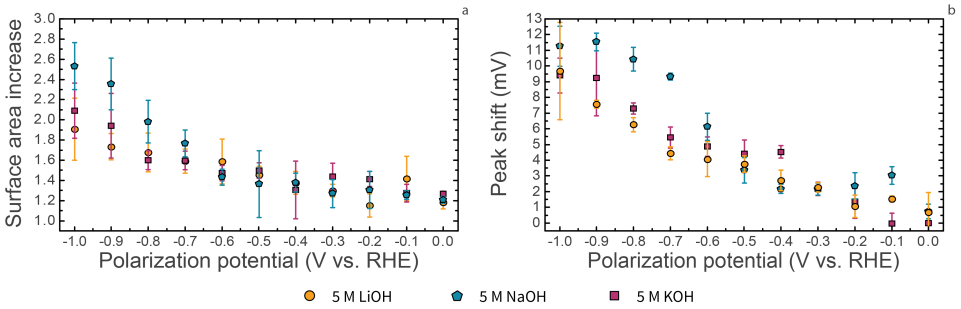

Fig. 4.5 | Relative rhodium surface area increase after cathodic polarization **(a)** and shift of the anodic hydrogen peak **(b)**, as a function of the applied polarization potential in 5 *M* LiOH, 5 *M* NaOH and 5 *M* KOH. Each data point is the average of at least 3 independent experiments. Error bars represent one standard deviation; if an error bar is not visible, it falls within its corresponding data point.

LiOH. In electron microscopy (Fig. 4.6 **a**, **d**), Rh electrodes corroded in this electrolyte typically exhibit no signs of cathodic corrosion: with the exception of one electrode (Fig. A.22 **c**), the electrodes only contain ridges and cracks that align with the electrode, which Chapter 3 showed to not be caused by cathodic corrosion.

More signs of corrosion are visible for rhodium electrodes corroded in 5 *M* KOH (Fig. 4.6 **c**, **f**), which is the electrolyte that ranks second in surface area creation. Interestingly, this electrolyte does not cause the formation of large etch pits, but instead creates a high coverage of small particles that are attached to the surface.

Finally, small particles can be observed after corrosion in 5 *M* NaOH (Fig. 4.6 **b**, **e**) and large quasi-rectangular pits are found after corrosion at and below −0.9 *V vs.* RHE. These pits match those created in 10 *M* NaOH, and are assigned to (100) site formation (Chapter 3). They therefore match the CV peak shift ((100) preference) in Fig. 4.5 being highest for corrosion in NaOH. Additionally, the etch pits are the largest features observed for rhodium in this study, which correlates well with the electrochemical surface area increase being largest for 5 *M* NaOH.

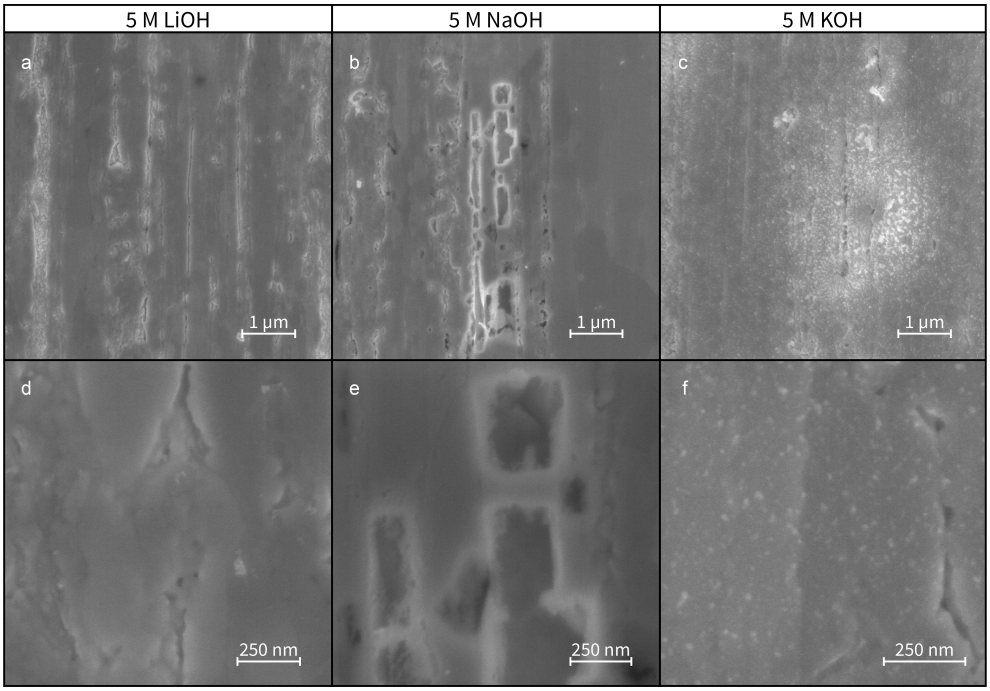

Fig. 4.6 | Scanning electron micrographs of Rh electrodes corroded at −1 *V vs.* RHE in *5 M* LiOH **(a**, **d)**, *5 M* NaOH **(b**, **e)** and *5 M* KOH **(c**, **f)**.

Summarizing, both electrochemistry and electron microscopy indicate the surface area increase to be smallest for LiOH, followed respectively by KOH and NaOH. Besides, electrochemistry indicates the largest amount of (100) sites to be formed in NaOH, which matches the occurrence of large, quasi-rectangular etch pits. Although these observations from CV and SEM lack the clear trends observed for platinum, both techniques produce mutually consistent results for the corrosion behavior of rhodium.

Gold

For gold, the change in surface orientation will be studied by using the oxide region in the cyclic voltammogram. This region is situated approximately between 1.35 and 1.75 *V vs.* RHE and contains several overlapping peaks corresponding to the following three basal planes:[48,49]

1. Au(111) produces a peak at 1.58 *V vs.* RHE.
2. Au(100) produces a peak at 1.42 *V vs.* RHE.

3. Au(110) produces a peak at 1.46 V *vs.* RHE.

Peaks corresponding to (100) and (111)/(110)-oriented steps are found respectively at 1.39 and 1.43 V *vs.* RHE.[48] Though some of the peaks are situated rather close to each other, they are reliable indicators of the amount of exposed basal planes.[16] The peaks will therefore be used to assess changes in the electrode surface after cathodic corrosion. As with rhodium, these changes are not reported for concentrations of 1 M; corrosion in these concentrations did not produce changes that were significant enough to reliably identify onset potentials and etching preferences.

Cation identity

Larger changes are observed for experiments in 5 M alkali metal hydroxides. For corrosion in these electrolytes, voltammograms before and after 60 seconds of corrosion at -1.5 V *vs.* RHE are shown in Fig. 4.7. The figure shows both the first (Panel **a**) and fourth (Panel **b**) voltammetric cycles after cathodic corrosion, because the electrode surface changes between cycles due to repetitive oxidation and reduction.[16] Such changes could obscure the difference between cations if only the fourth cycle were used for comparison. In addition, the displayed CVs are shown for a more negative corrosion potential (-1.5 V *vs.* RHE) than those shown for rhodium and platinum. This is because corrosion is significantly milder for gold, which causes smaller differences between the cations at less negative potentials; voltammograms of electrodes polarized around the corrosion onsets and at -3.0 V *vs.* RHE are available in Fig. A.13–A.15.

At -1.5 V *vs.* RHE, corrosion in all three electrolytes creates some extent of (111) features. These features, which are visible around 1.58 V *vs.* RHE, can be used to identify the onset potential of gold corrosion (Chapter 3). This analysis is presented in Fig. A.29, and indicates the onset potentials to be -0.9 V *vs.* RHE (-1.8 V *vs.* NHE) for 5 M LiOH and -0.8 V *vs.* RHE (-1.7 V *vs.* NHE) for 5 M NaOH and KOH. As for platinum and rhodium, these potentials are 0.1 to 0.2 V more negative than the corrosion onset potential found in Chapter 3 for 10 M NaOH: -0.7 V *vs.* RHE (-1.6 V *vs.* NHE). This indicates a later onset of cathodic corrosion for all three cations in more dilute electrolytes.

When the facet preference of the cations is compared, several interesting features stand out. These features are most clearly visible in the first cycle after corrosion (Fig.4.7 **a**). From this cycle, one can observe that LiOH induces the creation of only a small amount of (111) facets. Instead, the most-developed peak is the (100) peak at 1.41 V *vs.* RHE.

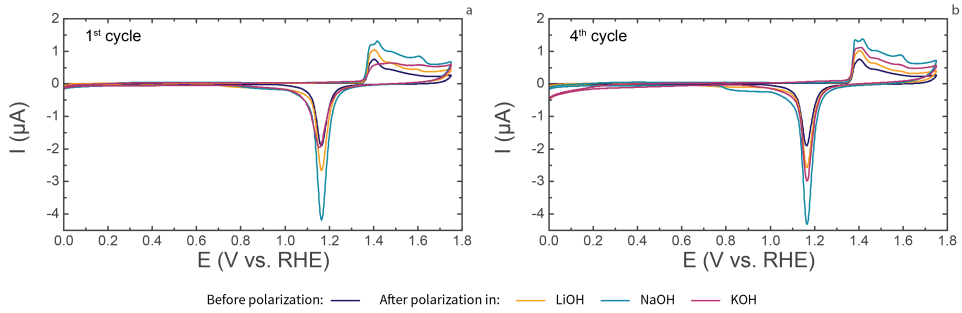

Fig. 4.7 | Cyclic voltammograms of Au, corroded in 5 *M* LiOH, 5 *M* NaOH and 5 *M* KOH at −1.5 *V vs.* RHE. CVs shown are the first cycle **(a)** and the fourth cycle **(b)** after cathodic corrosion. Voltammograms were recorded in 0.1 *M* H_2SO_4, at a scan rate of 50 $mV \cdot s^{-1}$.

This also holds true after 4 cycles (Fig. 4.7 **b**), with only small changes occurring between cycles.

The corrosion behavior in 5 *M* LiOH is not matched by NaOH, which induces a strong development of (111) sites (1.58 *V vs.* RHE) in both the first and fourth characterization cycles. An additional difference with respect to LiOH is the amount of created surface area, which can primarily be assessed by the size of the oxide reduction peak at 1.16 *V vs.* RHE.[50] A larger peak after corrosion in 5 *M* NaOH indicates significantly more surface area formation than corrosion in 5 *M* LiOH.

Finally, the created surface area in 5 *M* KOH displays interesting behavior with respect to the other two electrolytes. During the first cycle after corrosion, it appears that virtually no surface area has been created: the oxide reduction peak is similar in height to the peak of a pristine electrode. Interestingly, this peak grows in size during characterization after cathodic corrosion, leading to a CV similar to that after corrosion in 5 *M* LiOH, but with slightly more surface area, step sites, (110) terrace sites and (111) sites. Though these changes are discussed in more detail in Appendix A, the current analysis already indicates a strong difference in corrosion behavior for different cations.

As for Pt and Rh, these voltammetric changes correspond to changes observed with SEM. Scanning electron micrographs are shown for corrosion at −3.0 *V vs.* RHE in Fig. 4.8. This potential was chosen for SEM comparison because no corrosion could be detected by SEM for gold in 5 *M* LiOH at −1.5 *V vs.* RHE (Fig. A.25). For this electrolyte, corrosion features were only visible near the tip of the electrode. These features consist predominantly of etch pits, of which a particularly interesting example is shown in Panel **a**. This

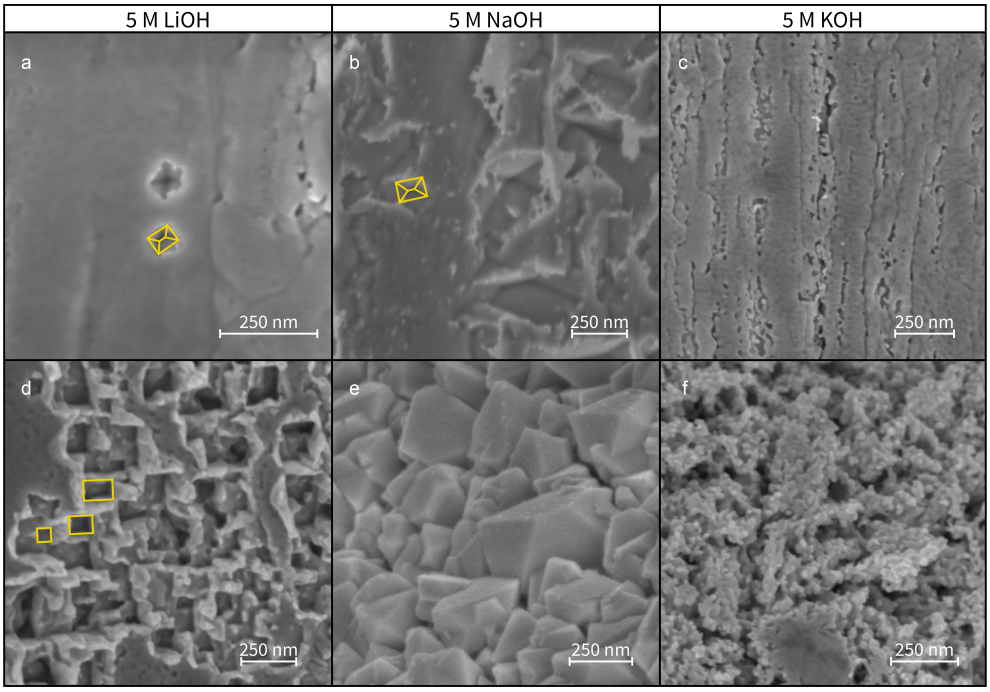

Fig. 4.8 | Scanning electron micrographs of Au electrodes corroded at −3 *V vs.* RHE in 5 *M* LiOH **(a**, **d)**, 5 *M* NaOH **(b**, **e)** and 5 *M* KOH **(c**, **f)**. Images in Panels **d**–**f** were taken at the tip of the electrode, whereas images in Panels **a**–**c** were taken further away from the tip. Representative etch pits have been highlighted in yellow.

type of etch pit is highlighted in yellow: it has outlines that appear to have roughly 90-degree angles and pit walls that slant inwards. This type of pit is therefore indicative of a (111)-type pit in a (100)-type surface, as can be rationalized using a model etch pit (Fig. A.28). In addition to these (111) sites, triangular and rectangular (100) pits are also visible in Fig. A.25 **c** and Fig. 4.8 **d**.

Pits are also observed after corrosion in 5 *M* NaOH, as is shown in Fig. 4.8 **b**. These features are larger than those seen for corrosion in 5 *M* LiOH, but match the orientation of (111)-type pits in (100)-type surfaces. The pits are accompanied by less well-defined roughness (Fig. A.26), but also by large, quasi-octahedral particles close to the tip of the electrode. These well-defined particles were previously observed after corrosion in 10 *M* NaOH and are strong indicators of the formation of (111) sites, as seen in Chapter 3.[8]

Well-defined particles and pits are absent for 5 *M* KOH. Corrosion in this electrolyte predominantly causes the etching of crystal grains, leading to the disordered features in

Fig. 4.8 **c**. In addition, cathodic corrosion creates disordered particles (Fig. 4.8 **f**); these particles are exclusively present at the tip of the electrode, where it is cut from the spool. As such, the presence of these small, disordered particles and etch pits supports the suggestion that corrosion in 5 *M* KOH causes the formation of a more disordered type of gold surface.

Thus, SEM imaging reinforces the electrochemical observations for gold corrosion, indicating the following behaviors for the three electrolytes. Firstly, 5 *M* LiOH is shown in both electrochemistry and electron microscopy to be the electrolyte in which the least surface area is created. When pronounced changes are present, both techniques can attribute them the formation of (triangular & rectangular) (100) sites and a small amount of (rectangular) (111) sites. Secondly, 5 *M* NaOH is shown electrochemically to create the most new surface area, consisting predominantly of (111) sites. This agrees well with the (111)-type etch pits and quasi-octahedral particles observed in SEM. Finally, 5 *M* KOH induces the formation of slightly more surface area than 5 *M* LiOH. This surface area appears to be disordered, as is indicated by the lack of well-defined oxide features in the first cycle after corrosion. The observed disorder is reflected in the SEM by the formation of many small etch pits and the presence of small nanoparticles at the tip of the electrode. As such, the combination of CV and SEM characterization paints a consistent picture of the corrosion behavior of gold in 5 *M* LiOH, NaOH and KOH.

Computationally derived adsorption and surface energies

After having experimentally mapped the corrosion behavior of Pt, Rh and Au, we exchange our experimental viewpoint for a computational perspective. From this perspective, we will first focus on the specific adsorption of alkali metal cations, followed by the surface energies of hydrogen-covered metals.

Specific adsorption of cations

We will focus first on the specific adsorption of Li^+, Na^+ and K^+ on Pt, Rh and Au. This approach extends from the work in Chapter 3 on sodium adsorption and initially considered adsorbed cations in vacuum, without including explicit solvation. However, explicit near-surface solvation was previously shown to significantly affect cation adsorption.[26] Explicit solvation was therefore included in the results in this chapter, whereas calculations without explicit solvation are shown for comparison in Fig. A.30–A.31. The presented calculations allowed us to calculate equilibrium adsorption potentials for cation

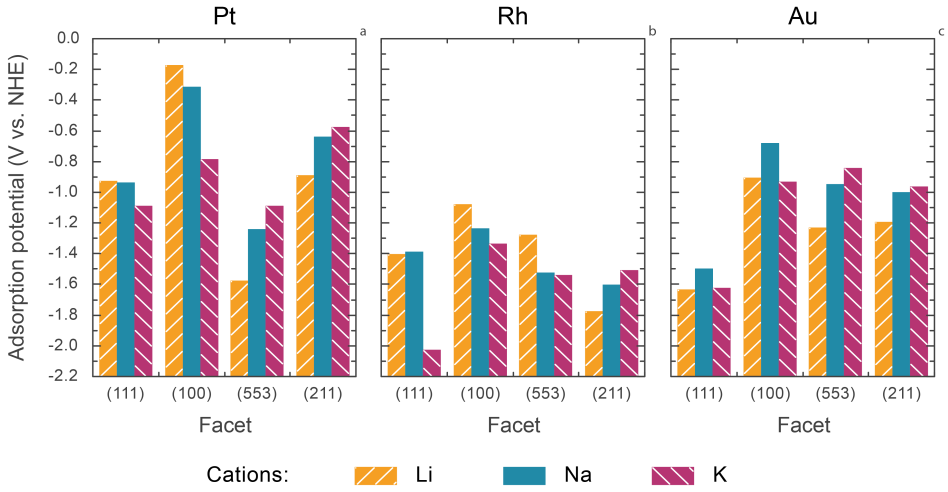

Fig. 4.9 | Equilibrium adsorption potentials for adsorption of Li, Na, and K on the (111), (100), (553) and (211) surfaces of Pt **(a)**, Rh **(b)**, and Au **(c)** from a 1 *M* solution of alkali metal cation.

adsorption, facilitating a direct comparison with the experimentally determined onset potentials.

Calculated equilibrium adsorption potentials for Li^+, Na^+, K^+ onto the (111), (100), (553) and (211) facets of Pt, Rh and Au are displayed in Fig. 4.9. In this figure, cation adsorption is energetically favorable at potentials below the indicated equilibrium adsorption potential, as is signified by the bars covering the entire cation adsorption potential range. Though the cations transfer only a small part of their charge to the surface upon adsorbing, they do lose part of their solvation shell and interact directly with the metal surface. This therefore means that, within the context of this work, the cations are specifically adsorbed in the range covered by the bars in Fig. 4.9.

Importantly, the adsorption range starts at less negative potentials than the onset potential of cathodic corrosion for most of the metal facets. Therefore, the cations are favorably adsorbed to the metal surface at potentials where cathodic corrosion occurs. As such, the results in Fig. 4.9 support the importance of cation specific adsorption during cathodic corrosion. However, further assessment of the role of cations requires closer examination of adsorption trends across the different metal surface facets and between each of the alkali metal cations.

The trend in adsorption between facets is strongest for platinum, see Fig. 4.9 **a**: cation

adsorption is weakest on (111)-type sites. This follows from the adsorption potential being most negative on the (111) and on the (553) facet.* This relatively weak binding to (111)-type sites is contrasted by adsorption on (100)-type sites: the least negative adsorption potentials are found for the (100) facet and the (211) facet.† This strong binding on (100) sites *vs.* (111) sites might be related to the more open nature of (100)-type sites, which causes stronger binding for a variety of adsorbates.[51–53] Interestingly, this would imply an even stronger binding on step sites *versus* terrace sites, which is not observed. This apparent discrepancy is caused by a difference in cation coverage, as is discussed in more detail in Appendix A. Nonetheless, both Pt steps and terraces bind cations favorably to (100)-type sites, which correlates well with the experimentally observed preference for the creation of (100) sites on platinum.

While the adsorption energies for platinum show a clear trend that favors adsorption on (100) sites, there is no straightforward facet trend for Rh and Au (Fig. 4.9 **b**, **c**). Although these metals match Pt in exhibiting a strong preference for adsorption on (100) terraces over (111) terraces, they generally lack the significant difference between (553) and (211) that Pt exhibits.

Similarly, Pt is the only metal to exhibit clear trends in the calculated differences between cations. For Pt, steps and terraces behave oppositely; on terraces, Li adsorbs most strongly, followed respectively by Na and K. In contrast, Pt steps adsorb K most strongly, followed respectively by Na and Li. This difference between terraces and stepped surfaces arises from the different relative coverages of the cations on each surface, as is explained in Appendix A.

The trends with respect to cation identity for platinum are only partly upheld for Rh and Au: only the Rh(100), Rh(211), Au(553) and Au(211) trends behave similarly to their Pt counterparts. This absence of a calculated trend matches the experimental absence of a clear facet trend between cations for both Rh and Au.

Energies of hydrogen-covered surfaces

In addition to examining alkali metal cation adsorption, we explored high coverages of adsorbed hydrogen which may be present on Pt, Rh and Au at cathodic corrosion potentials. We did so by calculating the surface energies of the (111) and (100) facets of

* (553) facets contain 5-atom long (111) terraces and (111) steps to which cations adsorb.

† (211) facets contain 3-atom long (111) terraces and (100) steps to which cations adsorb.

Pt, Rh and Au in the absence and presence of a monolayer (ML) of adsorbed hydrogen. These calculations were performed using values from literature DFT studies.[36,37] For (100) surfaces, we additionally found previously that the adsorption of as much as 1.25 monolayers of hydrogen is favorable at potentials near $0\ V$ *vs.* RHE.[40] This data was therefore included, and the surface energy extrapolated to lower potentials in Fig. 4.10 **a**. Similarly high coverages were calculated in the current work for Rh(100) and included in Fig. 4.10 **b**, since the hydrogen binding strength of Rh is similar to that of Pt. Because the calculations for $1.25\ ML$ coverage on Pt(100) and Rh(100) used different protocols than the calculations of Ferrin *et al.*, our results were added to the graph as separate lines. Interestingly, our DFT data in Fig. 4.10 (dark purple) and calculations using literature values (pink) appear similar. This agreement inspires confidence in using Fig. 4.10 as a first-order approximation of the stabilizing effect of adsorbed hydrogen.

Fig. 4.10 indicates that, at potentials positive of hydrogen adsorption, the surface energy is constant as a function of potential. This constant energy is a result of ignoring electrolyte species like water or hydroxyl, which may adsorb to strongly-binding surfaces and lower the overall surface energy at positive potentials. At more cathodic potentials, adsorbed hydrogen is calculated to be stable. These potentials generally correspond with hydrogen adsorption features in the blank cyclic voltammograms of platinum and rhodium and initiate a decrease in surface energy in Fig. 4.10. This linear energy decrease is driven by hydrogen adsorption. This adsorption is increasingly favorable at lower potentials, which lowers the total energy of the system. Eventually, this constant decrease causes the surface energy to drop below zero $eV \cdot \text{Å}^{-2}$, as compared to bulk metal. When this happens, the creation of more surface area to facilitate hydrogen adsorption is energetically more favorable than the breaking of Pt-Pt bonds that such creation of surface area would require.

Importantly, this surface energy transition occurs at potentials that match the experimental corrosion onset potentials: approximately -0.4 to $-0.5\ V$ *vs.* RHE for Pt and Rh, and $-0.7\ V$ *vs.* RHE for Au. (Exact potentials are given in Table A.1.) Though it is important to emphasize that we calculated the curves in Fig. 4.10 using literature data that was obtained using different DFT methodologies,[36,37] the curves match our experimentally determined onset potentials rather well. As such, Fig. 4.10 indicates that high hydrogen coverages may be an energetic driving force for surface area creation and could therefore strongly affect the onset of cathodic corrosion.

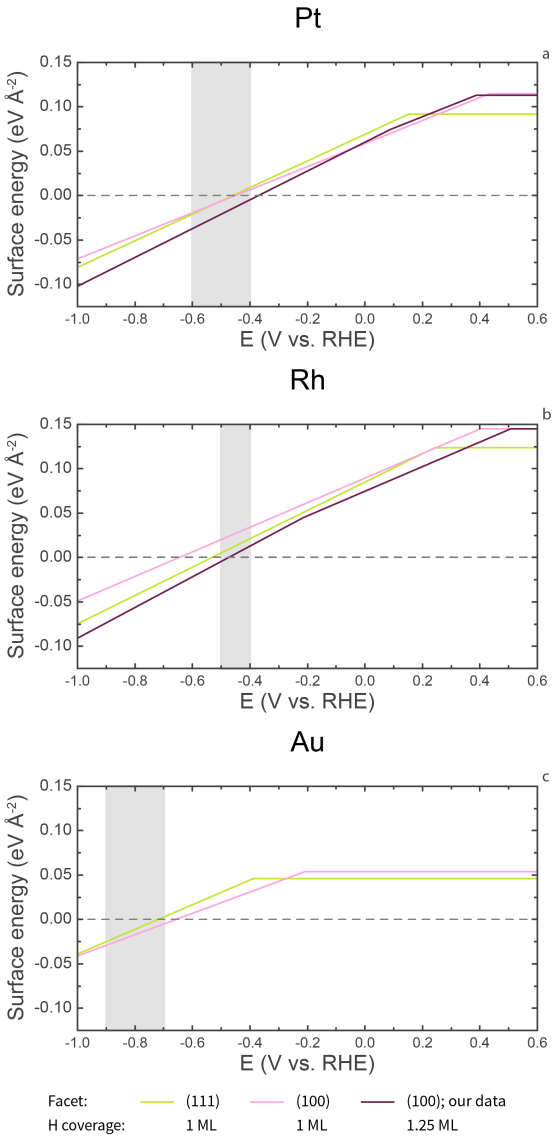

Fig. 4.10 | Potential-dependent surface energy of the (111) and (100) facets of Pt **(a)**, Rh **(b)**, and Au **(c)** in the absence and presence of 1 ML *H. On Pt(100) and Rh(100), we have additionally considered the adsorption of 1.25 ML *H. Our own data for Rh(100) was calculated with the PBE exchange-correlation functional instead of PW91. The range of experimentally determined onset potentials from this thesis is marked in grey.

4.3.2 Discussion

Onset potential

In the current chapter, we established onset potentials for cathodic corrosion of Pt, Rh and Au in various concentrations of LiOH, NaOH and KOH. Additionally, we explored the role of cation and hydrogen adsorption through theoretical calculations. Though this combination of theory and experiment does not unambiguously explain the nature of cathodic corrosion, it does provide valuable new clues towards elucidating this puzzling (electro)chemical phenomenon. Perhaps the most concrete of these clues are related to the onset potential of cathodic corrosion.

The onset potential depends strongly on the electrolyte concentration: corrosion takes place at less negative potentials as the concentration increases. This trend is valid for Pt, Rh and Au, as can be seen by comparing the current results with those in Chapter 2 & 3 for more concentrated electrolytes. The corrosion onset is similarly sensitive to the nature of the electrolyte cation: it generally starts at the least negative potentials for K^+, followed respectively by Na^+ and Li^+.

Though these experimental trends appear robust, they cannot conclusively be explained by the corresponding DFT results on cation adsorption. We therefore restrict this comparison of theory and experiment to two observations. First of all, larger cations are calculated to bind stronger to step edges. This could matter if cathodic corrosion were initiated at high-energy defect or step sites on the electrodes. Secondly, we calculate that larger cations retain more of their charge upon adsorption. This could shift the onset potential if cations were required to electrostatically stabilize an anionic reaction intermediate. Though speculative in nature, these computational suggestions parallel the observed effects of cations on the corrosion onset potential. These suggestions are therefore worthy of consideration in further mechanistic studies of cathodic corrosion.

In addition to the influence of cations on the corrosion onset, a similar role might be played by hydrogen: hydrogen is adsorbed on most metal surfaces at potentials where cathodic corrosion occurs. Exploring the effect of adsorbed hydrogen on the potential-dependent surface energy (Fig. 4.10), we found an energetic driving force for the creation of surface area. This driving force appears at potentials that correspond remarkably well with the experimental cathodic corrosion onset potentials. Importantly, this agreement was established without making any kinetic or mechanistic assumptions: it simply indicates a thermodynamic driving force for creating more surface area around the corrosion

onset potential.

The onset potential of cathodic corrosion therefore appears to depend on three major actors:

1. The corroded metal.

2. The electrolyte cation, which also affects various other factors of corrosion (Chapter 2 & 3).[9–13]

3. Adsorbed hydrogen.

Given the pronounced effect of each of these actors on the location of the corrosion onset, it is likely that each of them is involved in creating the elusive intermediate species that underlies cathodic corrosion. A possible class of species that contains all three actors and has been observed experimentally is ternary metal hydrides.

In brief, ternary metal hydrides are compounds with the general formula $A_xM_yH_z$, where A is an alkali or alkaline earth metal and M is a transition metal.[54] In the solid state, these compounds contain anionic $[MH_n]^{\delta-}$ clusters, which are stabilized by surrounding cations.[55] As such, these hydrides contain both ionic (or coulombic) interactions between the cation and the anionic cluster, and covalent (or coordination) bonds between the metal center and the hydrogen atoms.[56] A variety of these hydrides with Pt and Rh centers have been synthesized and fully characterized.[55,57] Though similar solid-state examples of ternary gold hydrides are unavailable, their existence is not unlikely: AuH_2^- and AuH_4^- have been generated with laser ablation,[58] and theoretical calculations suggest that such AuH_2^- clusters could be stabilized by alkali metal cations.[59] Given these examples of ternary hydrides of Pt, Rh and Au, such compounds might be the elusive intermediate that underlies cathodic corrosion.

The presence of these species would match the suggested simultaneous importance of the corroded metal, electrolyte cations and adsorbed hydrogen. However, ternary metal hydrides are extremely sensitive to moisture and air,[55,60] which would make them highly unstable in our working electrolyte. Interestingly, this instability is consistent with current and previous experimental results. After all, during cathodic corrosion, only the reacting material (e.g. Pt, Rh, Au) and produced material (e.g. corroded Pt, Rh & Au surfaces and nanoparticles) have explicitly been identified: the intermediate species is highly unstable and has, as of now, escaped direct detection and chemical isolation.

In short, these hydrides are unstable enough to explain their elusiveness during experiments, yet have been studied and characterized to such an extent that their existence is plausible in our system. Additionally, they require the presence of a metal center, hydrogen *and* a stabilizing cation. As such, these hydrides are, in our opinion, prime targets for future mechanistic studies of the reaction intermediates of cathodic corrosion.

Electrode area and facet distribution

Besides considering these mechanistic insights, it is instructive to evaluate the role of cations in the final surface structure of the corroded electrodes. This role is relatively clear when considering cation concentration: higher concentrations lead to more severe changes in the facet distribution and the amount of created surface area for Pt (Fig. 4.1 & 4.2). Rh and Au behave similarly in that corrosion is rather mild at lower cation concentrations.

These effects of cation concentration appear to be thermodynamic in nature, meaning here that prolonged corrosion in dilute electrolytes is not likely to produce similar results as shorter corrosion in more concentrated electrolytes. This is illustrated by the corrosion of electrodes in $5\ M$ NaOH for various amounts of time (Fig. A.32): the difference between 1 and 10 minutes of corrosion is minimal, if at all present. As such, the presented corroded electrodes appear to have reached a stable state and the differences in Fig. 4.1 are strictly a consequence of the cation concentration.

Similar to the cation concentration, the cation identity also affects the final state of the corroded electrodes. However, this effect appears to vary with the applied potential. At the most negative potentials, both the facet distribution and surface area creation are strongly affected by the cation identity for all three metals.

The strongest trend in facet preference is observed for the corrosion of Pt: a monotonic (100) preference is observed when increasing the cation size in $1\ M$ electrolyte concentrations. This trend is captured well by our DFT results, which indicate the strongest binding on (100)-type steps ((211) facets) for K, followed by Na and Li. This trend is matched by (110)-type steps ((553) facets), which might explain why more step sites and more general surface area are produced in $5\ M$ KOH, compared to LiOH and NaOH. As such, the DFT results for cation adsorption agree well with the experimental corrosion behavior of Pt.

However, the calculated cation adsorption strengths match less well with the corrosion behavior of Rh and Au: they do not explain the observed facet distributions or why

most area is created in NaOH. At best, the absence of a clear trend in DFT resembles the absence of a clear trend in experimental facet distribution. The lack of overlap between experiment and theory can be attributed to the calculations in Fig. 4.9 only capturing cation adsorption. Other factors, like hydrogen adsorption, are not captured in these calculations. Cation adsorption therefore only partly determines the corrosion behavior at more negative potentials and hydrogen co-adsorption might improve the predictions.

At milder negative potentials, the cation identity appears unimportant in determining the electrode structure for all three metals:

- For Pt, the CVs of electrodes corroded at mildly negative potentials show great similarity (Fig. 4.3), especially when comparing the amount of created (100) terraces. In addition, close comparison of the micrographs in Fig. 4.2, Fig. 4.4 and Fig. A.16–A.21 reveals that the earliest indications of corrosion are typically (100)-oriented triangular etch pits, regardless of the identity and concentration of the electrolyte cation.

- For Rh, both the surface area increase and hydrogen desorption peak shift (Fig. 4.5) are similar for all three electrolytes at mildly negative potentials (approximately $-0.6\ V$ *vs.* RHE) before diverging at more negative potentials.

- For Au, the facet distribution after corrosion (Fig. A.29) is virtually identical for corrosion in both $5\ M$ NaOH and KOH.

These observations suggest that the cation is of limited relevance in determining the electrode structure at mildly negative potentials, but of large significance at more negative potentials. This might be due to an increased adsorbed cation coverage at more negative potentials, as is explained in Appendix A. Such a coverage dependence might imply an interplay between both adsorbed cations and adsorbed hydrogen. This would be consistent with our mechanistic hypothesis regarding ternary metal hydrides.

Implications for electrode structuring

Regardless of the exact mechanisms that underlie the final structure of corroded electrodes, the current work provides a detailed characterization of the cathodic corrosion behavior of various combinations of electrode materials and electrolyte alkali metal cations. These results are particularly relevant when employing cathodic corrosion to

alter the surface of metallic electrodes. Hence, we will end our discussion with recommendations for structuring electrodes by cathodic corrosion. The first three sets of recommendations are metal-specific:

- Platinum generally prefers forming (100) sites during cathodic corrosion. However, the extent of this preference can be significantly tuned by varying both the identity and concentration of the alkali metal cations in the electrolyte. The strongest preference for forming well-defined (100) terraces without creating steps is found for corrosion in $5\ M$ NaOH. If LiOH is used instead, the corroded electrodes appear smoother in SEM (Fig. 4.4, Fig. A.16 and Fig. A.19) and expose slightly less (100) terraces in voltammetry. Accordingly, changing the cation to K^+ induces the formation a rougher and (at $5\ M$ concentrations) more disordered surface.

- Rhodium exhibits a minor (100) preference, which is strongest in NaOH. NaOH is also the electrolyte of choice when a large surface area increase is desired. If less surface area and (100) preference are required, LiOH and KOH are more appropriate working electrolytes: corrosion in LiOH creates surfaces that appear in SEM to retain most of their original morphology, while KOH induces nano-sized corrugation and slightly more roughness on the electrode.

- For gold, cathodic corrosion should be carried out at more negative potentials than for platinum and rhodium. When doing so, corrosion in LiOH creates electrodes with moderate roughening, exhibiting some well-defined (100) and (111) etch pits. More severe roughening is present after corrosion in NaOH, which creates most roughening and large (111)-oriented particles. Newly formed (111) sites are most clearly expressed in $10\ M$ NaOH, where the (111) oxide peak can be quite well-defined (Chapter 3). Finally, corrosion in KOH creates intermediate degrees of surface area, accompanied by corrugation along grain boundaries.

Finally, we will conclude our recommendations with three more general notes:

- Both this chapter and Chapter 2 & 3 indicate crystallographic preferences in cathodic corrosion: clear facet preferences can be identified and corrosion appears most pronounced around grain boundaries and, in case of un-annealed Rh & Au electrodes, in areas close to where the electrodes were cut from the spool with wire cutters. This parallels previous findings in nanoparticle synthesis through cathodic corrosion, which achieved the most well-defined nanoparticles after pro-

longed annealing of the parent electrode.[12] The extent of corrosion may therefore vary, depending on the initial state of the electrode: more or less corrosion than found in the current work may be observed if mechanical stress is reduced by annealing or introduced by methods like mechanical polishing.

- Our recommendations are strictly valid in the studied potential range. Though more negative potentials will likely just emphasize the findings in the current work, exploring such potentials is encouraged when aiming to create an optimal surface structure. Similarly, if the target surface structure requires less corrosion, lower potentials can be chosen by consulting Fig. A.4 through Fig. A.27.

- Though the current work focuses on using pure alkali metal hydroxides to avoid overcomplicated analyses, different electrolytes might generate different and interesting results. Mixing cations to combine or balance their effects might be effective, as well as using entirely different cations. However, care should be taken not to choose cations that electrodeposit under the chosen corrosion conditions, in order to avoid the possible formation of metal overlayers or even alloy phases.[61]

4.4 Conclusions

The current work has explored the cathodic corrosion behavior of Pt, Rh and Au in LiOH, NaOH and KOH, in order to systematically assess the effect of the electrolyte cation. In doing so, it was found experimentally that both the concentration and identity of the cation can strongly affect the surface area and facet distribution of corroded electrodes, as well as the cathodic corrosion onset potential. These experimental results led to a set of concrete recommendations for employing cathodic corrosion to modify the structure of metallic electrodes for a specific purpose.

In addition to producing guidelines, we rationalized our experimental results by using first-principles calculations of cation adsorption. Importantly, the calculations indicate that cations are adsorbed at potentials where cathodic corrosion occurs. Though the calculations also satisfactorily reproduce the trend for (100) site formation for Pt in 1 M LiOH, NaOH and KOH, they do not conclusively explain other trends in the onset potential, facet distribution and surface area increase after cathodic corrosion. More mechanistic information on cathodic corrosion is therefore required to explain the strong effect of cations on these factors.

Equally relevant for the onset of corrosion is perhaps the adsorption of hydrogen; an analysis of literature hydrogen adsorption values indicates a thermodynamic driving force for the creation of surface area. Importantly, this driving force matches the experimental trend in onset potentials between metals, *without* making any mechanistic assumptions.

By combining the observed relevance of hydrogen, electrolyte cations and the corroded electrode material, we postulate that the key reaction intermediate of cathodic corrosion might be a ternary metal hydride. Though the current work provides no direct evidence for such metal hydrides, their solid-state properties have been extensively studied and their occurrence would match several experimental observations. Notably, ternary metal hydrides would explain the importance of cations that has been explored in previous work and reaffirmed in the presented research. Ternary metal hydrides are therefore plausible reaction intermediates, which could serve as a starting point for further mechanistic studies of cathodic corrosion.

In conclusion, the current work on cathodic corrosion provides recommendations for electrode surface structuring, extensive information on the role of cations during DC cathodic corrosion and a testable hypothesis for the nature of the elusive cathodic corrosion reaction intermediate. As such, the work presented here is an essential step in both understanding and applying cathodic corrosion.

4.5 Acknowledgements

The use of supercomputing facilities at SURFsara was sponsored by NWO Physical Sciences, with financial support by NWO. SEM measurements were performed at the shared clean room facility at the Leiden Institute of Physics.

References

1. Haber, F. The Phenomenon of the Formation of Metallic Dust from Cathodes. *Transactions of the American Electrochemical Society* **2,** 189–196 (1902).
2. Kabanov, B. N., Astakhov, I. I. & Kiseleva, I. G. Formation of crystalline intermetallic compounds and solid solutions in electrochemical incorporation of metals into cathodes. *Electrochimica Acta* **24,** 167–171 (1979).
3. Liu, J., Huang, W., Chen, S. & Hu, S. Facile electrochemical dispersion of bulk Rh into hydrosols. *Int. J. Electrochem. Sci.* **4,** 1302–1308 (2009).
4. Huang, W., Chen, S., Zheng, J. & Li, Z. Facile preparation of Pt hydrosols by dispersing bulk Pt with potential perturbations. *Electrochemistry Communications* **11,** 469–472 (2009).

5. Leontyev, I., Kuriganova, A., Kudryavtsev, Y., Dkhil, B. & Smirnova, N. New life of a forgotten method: Electrochemical route toward highly efficient Pt/C catalysts for low-temperature fuel cells. *Applied Catalysis A: General* **431-432,** 120–125 (2012).
6. Yanson, A. I. *et al.* Cathodic Corrosion: A Quick, Clean, and Versatile Method for the Synthesis of Metallic Nanoparticles. *Angewandte Chemie International Edition* **50,** 6346–6350 (2011).
7. Gangal, U., Srivastava, M. & Sen Gupta, S. K. Mechanism of the Breakdown of Normal Electrolysis and the Transition to Contact Glow Discharge Electrolysis. *Journal of The Electrochemical Society* **156,** F131–F136 (2009).
8. Strasser, P., Gliech, M., Kuehl, S. & Moeller, T. Electrochemical processes on solid shaped nanoparticles with defined facets. *Chemical Society Reviews* **47,** 715–735 (2018).
9. Yanson, A., Antonov, P., Rodriguez, P. & Koper, M. Influence of the electrolyte concentration on the size and shape of platinum nanoparticles synthesized by cathodic corrosion. *Electrochimica Acta* **112,** 913–918 (2013).
10. Yanson, A., Antonov, P., Yanson, Y. & Koper, M. Controlling the size of platinum nanoparticles prepared by cathodic corrosion. *Electrochimica Acta* **110,** 796–800 (2013).
11. Feng, J. *et al.* Cathodic Corrosion of a Bulk Wire to Nonaggregated Functional Nanocrystals and Nanoalloys. *ACS Applied Materials & Interfaces* **10,** 9532–9540 (2018).
12. Duca, M., Rodriguez, P., Yanson, A. I. & Koper, M. T. M. Selective Electrocatalysis on Platinum Nanoparticles with Preferential (100) Orientation Prepared by Cathodic Corrosion. *Topics in Catalysis* **57,** 255–264 (2014).
13. Yanson, A. I. & Yanson, Y. I. Cathodic corrosion. II. Properties of nanoparticles synthesized by cathodic corrosion. *Low Temperature Physics* **39,** 312–317 (2013).
14. Peng, Z. & Yang, H. Designer platinum nanoparticles: Control of shape, composition in alloy, nanostructure and electrocatalytic property. *Nano Today* **4,** 143–164 (2009).
15. Van de Krol, R. in *Photoelectrochemical Hydrogen Production* (eds Van de Krol, R. & Grätzel, M.) 109 (Springer, Boston, MA, 2012).
16. Jeyabharathi, C., Ahrens, P., Hasse, U. & Scholz, F. Identification of low-index crystal planes of polycrystalline gold on the basis of electrochemical oxide layer formation. *Journal of Solid State Electrochemistry* **20,** 3025–3031 (2016).
17. Kresse, G. Ab initio molecular dynamics for liquid metals. *Journal of Non-Crystalline Solids* **192-193,** 222–229 (1995).
18. Kresse, G. & Furthmüller, J. Efficiency of ab-initio total energy calculations for metals and semiconductors using a plane-wave basis set. *Computational Materials Science* **6,** 15–50 (1996).
19. Kresse, G. & Furthmüller, J. Efficient iterative schemes for ab initio total-energy calculations using a plane-wave basis set. *Physical Review B* **54,** 11169–11186 (1996).
20. Perdew, J. P., Burke, K. & Ernzerhof, M. Generalized Gradient Approximation Made Simple. *Physical Review Letters* **77,** 3865–3868 (1996).
21. Perdew, J. P., Burke, K. & Ernzerhof, M. Generalized Gradient Approximation Made Simple [Phys. Rev. Lett. 77, 3865 (1996)]. *Physical Review Letters* **78,** 1396–1396 (1997).
22. Blöchl, P. E. Projector augmented-wave method. *Physical Review B* **50,** 17953–17979 (1994).
23. Kresse, G. & Joubert, D. From ultrasoft pseudopotentials to the projector augmented-wave method. *Physical Review B* **59,** 1758–1775 (1999).
24. Monkhorst, H. J. & Pack, J. D. Special points for Brillouin-zone integrations. *Physical Review B* **13,** 5188–5192 (1976).
25. Bengtsson, L. Dipole correction for surface supercell calculations. *Physical Review B - Condensed Matter and Materials Physics* **59,** 12301–12304 (1999).
26. Mills, J. N., McCrum, I. T. & Janik, M. J. Alkali cation specific adsorption onto fcc(111) transition metal electrodes. *Phys. Chem. Chem. Phys.* **16,** 13699–13707 (2014).
27. McCrum, I. T. & Janik, M. J. pH and Alkali Cation Effects on the Pt Cyclic Voltammogram Explained Using Density Functional Theory. *The Journal of Physical Chemistry C* **120,** 457–471 (2016).
28. Ogasawara, H. *et al.* Structure and Bonding of Water on Pt(111). *Physical Review Letters* **89,** 276102 (2002).

29. He, Z.-D., Hanselman, S., Chen, Y.-X., Koper, M. T. M. & Calle-Vallejo, F. Importance of Solvation for the Accurate Prediction of Oxygen Reduction Activities of Pt-Based Electrocatalysts. *The Journal of Physical Chemistry Letters* **8,** 2243–2246 (2017).
30. Han, B., Viswanathan, V. & Pitsch, H. First-Principles Based Analysis of the Electrocatalytic Activity of the Unreconstructed Pt(100) Surface for Oxygen Reduction Reaction. *The Journal of Physical Chemistry C* **116,** 6174–6183 (2012).
31. Kolb, M. J. *et al.* Double-Stranded Water on Stepped Platinum Surfaces. *Physical Review Letters* **116,** 136101 (2016).
32. Momma, K. & Izumi, F. VESTA 3 for three-dimensional visualization of crystal, volumetric and morphology data. *Journal of Applied Crystallography* **44,** 1272–1276 (2011).
33. Varma, S. & Rempe, S. B. Coordination numbers of alkali metal ions in aqueous solutions. *Biophysical Chemistry* **124,** 192–199 (2006).
34. Resasco, J. *et al.* Promoter Effects of Alkali Metal Cations on the Electrochemical Reduction of Carbon Dioxide. *Journal of the American Chemical Society* **139,** 11277–11287 (2017).
35. Pérez-Gallent, E., Marcandalli, G., Figueiredo, M. C., Calle-Vallejo, F. & Koper, M. T. M. Structure- and Potential-Dependent Cation Effects on CO Reduction at Copper Single-Crystal Electrodes. *Journal of the American Chemical Society* **139,** 16412–16419 (2017).
36. Tran, R. *et al.* Surface energies of elemental crystals. *Scientific Data* **3,** 160080 (2016).
37. Ferrin, P., Kandoi, S., Nilekar, A. U. & Mavrikakis, M. Hydrogen adsorption, absorption and diffusion on and in transition metal surfaces: A DFT study. *Surface Science* **606,** 679–689 (2012).
38. Karlberg, G. S. *et al.* Cyclic Voltammograms for H on Pt(111) and Pt(100) from First Principles. *Physical Review Letters* **99,** 126101 (2007).
39. Skúlason, E. *et al.* Modeling the Electrochemical Hydrogen Oxidation and Evolution Reactions on the Basis of Density Functional Theory Calculations. *The Journal of Physical Chemistry C* **114,** 22374–22374 (2010).
40. McCrum, I. T., Hickner, M. A. & Janik, M. J. First-Principles Calculation of Pt Surface Energies in an Electrochemical Environment: Thermodynamic Driving Forces for Surface Faceting and Nanoparticle Reconstruction. *Langmuir* **33,** 7043–7052 (2017).
41. Koper, M. T. & Lukkien, J. J. Modeling the butterfly: the voltammetry of $(\sqrt{3} \times \sqrt{3})$R30° and p$(2 \times 2)$ overlayers on (111) electrodes. *Journal of Electroanalytical Chemistry* **485,** 161–165 (2000).
42. Garcia-Araez, N., Lukkien, J. J., Koper, M. T. & Feliu, J. M. Competitive adsorption of hydrogen and bromide on Pt(100): Mean-field approximation vs. Monte Carlo simulations. *Journal of Electroanalytical Chemistry* **588,** 1–14 (2006).
43. Solla-Gullón, J., Rodríguez, P., Herrero, E., Aldaz, A. & Feliu, J. M. Surface characterization of platinum electrodes. *Phys. Chem. Chem. Phys.* **10,** 1359–1373 (2008).
44. Chen, X., McCrum, I. T., Schwarz, K. A., Janik, M. J. & Koper, M. T. M. Co-adsorption of Cations as the Cause of the Apparent pH Dependence of Hydrogen Adsorption on a Stepped Platinum Single-Crystal Electrode. *Angewandte Chemie International Edition* **56,** 15025–15029 (2017).
45. McCrum, I. T. & Janik, M. J. First Principles Simulations of Cyclic Voltammograms on Stepped Pt(553) and Pt(533) Electrode Surfaces. *ChemElectroChem* **3,** 1609–1617 (2016).
46. Vidal-Iglesias, F. J., Arán-Ais, R. M., Solla-Gullón, J., Herrero, E. & Feliu, J. M. Electrochemical Characterization of Shape-Controlled Pt Nanoparticles in Different Supporting Electrolytes. *ACS Catalysis* **2,** 901–910 (2012).
47. Xu, Q., Linke, U., Bujak, R. & Wandlowski, T. Preparation and electrochemical characterization of low-index rhodium single crystal electrodes in sulfuric acid. *Electrochimica Acta* **54,** 5509–5521 (2009).
48. Štrbac, S., Adžić, R. & Hamelin, A. Oxide formation on gold single crystal stepped surfaces. *Journal of Electroanalytical Chemistry and Interfacial Electrochemistry* **249,** 291–310 (1988).
49. Kibler, L. A. *Preparation and Characterization of Noble Metal Single Crystal Electrode Surfaces* 2003.
50. Trasatti, S. & Petrii, O. Real surface area measurements in electrochemistry. *Pure and applied chemistry* **63,** 711–734 (1991).

51. Li, H. *et al.* Why (1 0 0) Terraces Break and Make Bonds: Oxidation of Dimethyl Ether on Platinum Single-Crystal Electrodes. *Journal of the American Chemical Society* **135,** 14329–14338 (2013).
52. Li, H., Li, Y., Koper, M. T. M. & Calle-Vallejo, F. Bond-Making and Breaking between Carbon, Nitrogen, and Oxygen in Electrocatalysis. *Journal of the American Chemical Society* **136,** 15694–15701 (2014).
53. Calle-Vallejo, F., Loffreda, D., Koper, M. T. M. & Sautet, P. Introducing structural sensitivity into adsorption–energy scaling relations by means of coordination numbers. *Nature Chemistry* **7,** 403–410 (2015).
54. Firman, T. K. & Landis, C. R. Structure and Electron Counting in Ternary Transition Metal Hydrides. *Journal of the American Chemical Society* **120,** 12650–12656 (1998).
55. Yvon, K. & Renaudin, G. in *Encyclopedia of Inorganic Chemistry* (eds King, R. B., Crabtree, R. H., Lukehart, C. M., Atwood, D. A. & Scott, R. A.) 2nd ed., 1814–1846 (John Wiley & Sons, Ltd, Chichester, UK, 2006).
56. Orgaz, E. & Gupta, M. Chemical bonding features of the ternary alkali metal platinum and palladium hydrides. *International Journal of Quantum Chemistry* **80,** 141–152 (2000).
57. Bronger, W., Müller, P., Schmitz, D. & Spittank, H. Synthese und Struktur von Na2PtH4, einem ternären Hydrid mit quadratisch planaren PtH42-Baugruppen. *Zeitschrift für anorganische und allgemeine Chemie* **516,** 35–41 (1984).
58. Wang, X. & Andrews, L. Gold Is Noble but Gold Hydride Anions Are Stable. *Angewandte Chemie International Edition* **42,** 5201–5206 (2003).
59. Rahm, M., Hoffmann, R. & Ashcroft, N. W. Ternary Gold Hydrides: Routes to Stable and Potentially Superconducting Compounds. *Journal of the American Chemical Society* **139,** 8740–8751 (2017).
60. Suchanek, E., Lange, N., Auffermann, G., Bronger, W. & Lutz, H. D. Raman spectroscopic studies on palladium and platinum hydrido complexes. *Journal of Raman Spectroscopy* **30,** 981–986 (1999).
61. Bennett, E. *et al.* A Synthetic Route for the Effective Preparation of Metal Alloy Nanoparticles and Their Use as Active Electrocatalysts. *ACS Catalysis* **6,** 1533–1539 (2016).